chemosensors

Article

Green Synthesis of ZnO Nanoparticles Using *Retama raetam* Leaf Extract for VOC Sensing Applications

Tarek Sekrafi [1], Mosaab Echabaane [1], Ahmadou Ly [2], Marc Debliquy [3], Chérif Dridi [1] and Driss Lahem [2,*]

[1] NANOMISENE Laboratory LR16CRMN01, Center for Research on Microelectronics and Nanotechnology of Sousse, Technopark of Sousse, B. P. 334, Sousse 4050, Tunisia
[2] Materia Nova, Materials R&D Centre, Parc Initialis, Avenue Nicolas Copernic 3, 7000 Mons, Belgium
[3] Materials Science Unit, University of Mons, Rue de l'Epargne 56, 7000 Mons, Belgium
* Correspondence: driss.lahem@materianova.be

Abstract

The green synthesis of zinc oxide nanoparticles (ZnO NPs) using *Retama raetam* leaf extract via microwave irradiation was investigated. The biosynthesized NPs were characterized using scanning electron microscopy (SEM), energy dispersive X-ray spectroscopy (EDS), X-ray diffraction (XRD), Fourier transform infrared spectroscopy (FTIR), and UV-Vis spectrophotometry. An XRD pattern confirmed the formation of a hexagonal wurtzite structure. An FTIR analysis indicated the interactions of the NPs with bioactive molecules involved in their synthesis. SEM and STEM imaging determined the morphology of the NPs with an average size of 14 nm. Furthermore, the biosynthesized ZnO NPs were used as a sensitive layer for detecting volatile organic compounds (VOCs) at low concentrations ranging from 0.5 to 5 ppm. The response sensor measured at an optimum operating temperature of 250 °C and 50% relative humidity (RH). The sensor exhibited a strong response to 5 ppm ethanol (325%), a detection limit as low as 4 ppb and an excellent stability across varying humidity levels.

Keywords: green synthesis; *Retama raetam*; ZnO NPs; VOCs; low concentrations; gas sensor

1. Introduction

The monitoring of volatile organic compounds (VOCs) is essential to maintaining indoor air quality (IAQ). Higher concentrations of VOCs such as acetone, isopropanol, and ethanol are often detected, as these are the main components of cleaning agents, disinfectants, and solvents [1,2]. Formaldehyde is predominantly emitted from common household sources, including flooring, wooden furniture, and paint [3]. Long-term exposure to VOCs could cause severe damage to the respiratory and immune systems, causing conditions such as cancer, neurological disorders, and other chronic and life-threatening diseases [4]. Consequently, a sensitive VOC sensing system becomes a key tool for public safety in environments like classrooms, homes, offices, and factories. Most gas sensors operate on the principle of changing the concentration of a target gas present in the atmosphere into an electrical signal, which is conventionally measured as change in voltage, current, or resistance. Metal oxide semiconductors for gases have gained a lot of research attention thanks to their high sensitivity, low cost, simple fabrication process, and extremely good compatibility with modern electronic technologies [5]. ZnO, in particular, is widely used in gas detection applications due to its advantageous properties, including a wide bandgap, high chemical stability, favorable band positioning, and non-toxicity [6].

Check for updates

Received: 19 December 2025
Revised: 28 January 2026
Accepted: 31 January 2026
Published: 4 February 2026

Copyright: © 2026 by the authors. Licensee MDPI, Basel, Switzerland. This article is an open access article distributed under the terms and conditions of the Creative Commons Attribution (CC BY) license.

These characteristics make ZnO a great material for the fabrication of efficient and reliable gas sensors [7].

Various methods for the preparation of ZnO have been established, including sol–gel [8], hydrothermal [9], spray pyrolysis [10], and microwave-assisted techniques [11]. Among these methods, the microwave-assisted method offers several benefits over conventional heating, such as faster reaction rates, uniform particle size distribution, and higher yield [12]. For ZnO NP synthesis, most conventional methods rely on a variety of chemical precursors and additional reagents; however, green synthesis offers a one-step, cost-effective, eco-friendly, and pollution-free alternative [13]. This method is efficient in terms of time, energy consumption, and chemical safety, while also producing uniform nanostructures with high yield compared to other techniques.

Plant extracts provide biomolecules that are safe, green, cheap, and naturally available [14,15]. The biomolecules found in the extracts act as both reducing and stabilizing agents due to the presence of phytochemicals such as polyphenolic compounds, vitamins, alkaloids, amino acids, and terpenoids [16,17], which affect the properties and morphologies of the resulting nanomaterials [10].

ZnO NPs have been biosynthesized from several plant extracts (PEs) such as *Elaeagnus angustifolia* [18], *Pistia stratiotes* [19], *Acacia caesia* [20], *Allium sativum* [21], *Moringa oleifera* [22], *Cayratia pedate* [23], *Melia azedarach* [24], *Opuntia ficus-indica* [25], and *Ocimum tenuiflorum* [26].

Retama raetam is a spontaneous shrub belonging to the Fabaceae family, commonly known as R'tem in Tunisia. This plant has been traditionally utilized for the treatment of various ailments across many regions of the Mediterranean Basin and is one of the most widely applied species [27,28]. From the qualitative examination of PEs, it is obvious that the extracts contain phenolics, alkaloids, and flavonoids and boast strong antioxidant activity [29,30]. These findings motivated us to select *R. raetam* for the present study. To our knowledge, this is the first report on the green synthesis of ZnO NPs mediated by *R. raetam*.

In this study, we report the green approach for ZnO nanoparticle synthesis utilizing a leaf extract of *R. raetam* with a low-cost, efficient, simple, and rapid microwave-assisted combustion method. The synthesized ZnO NPs were characterized with a variety of techniques, including UV-Vis spectrometry, FTIR, XRD, SEM, EDX, and STEM. These techniques authenticate the structural and functional characteristics of the nanoparticles, implying that *R. raetam* is a potential sustainable resource in green nanoparticle synthesis. The developed sensor was tested for its electrical sensing performance under low concentrations of ethanol, isopropanol, acetone, and formaldehyde.

2. Materials and Methods

2.1. Preparation of the Extract

Fresh leaves of *R. raetam* were collected from Tataouine, Tunisia, in March 2024. The leaves were thoroughly cleaned and air-dried at 25 °C. Following drying and fine chopping, 20 g of the leaves was heated in 200 mL of distilled water (DW) at 80 °C for 10 min, after which the mixture was filtered to remove plant residues and impurities and the filtrate stored for subsequent use.

2.2. Green Synthesis of ZnO NPs

The ZnO NPs were synthesized via an eco-friendly green microwave-assisted combustion method utilizing the extract of *R. raetam*. Initially, the plant extract was prepared as described in previous protocols. Subsequently, 20 mL of the extract was transferred to a beaker and heated to 80 °C. Then, 3 g of zinc acetate dihydrate ($Zn(CH_3COO)_2 \cdot 2H_2O$, 99%) was introduced. The reaction mixture was agitated continuously with a magnetic agitator

until the precursor was completely dissolved. Then, the solution was placed in a domestic microwave oven operating at a fixed maximum power of 800 W for 3 min, which was sufficient to complete the reaction and obtain reproducible products. While the solution was nearing spontaneous combustion, it vaporized instantly and converted into fine and dry crystalline oxide powder where enormous amounts of gas were generated. Eventually, the powder obtained after this was calcined in a muffle furnace at 500 °C for 4 h under air. Figure 1 outlines the key steps of the green synthesis protocol employed in this study.

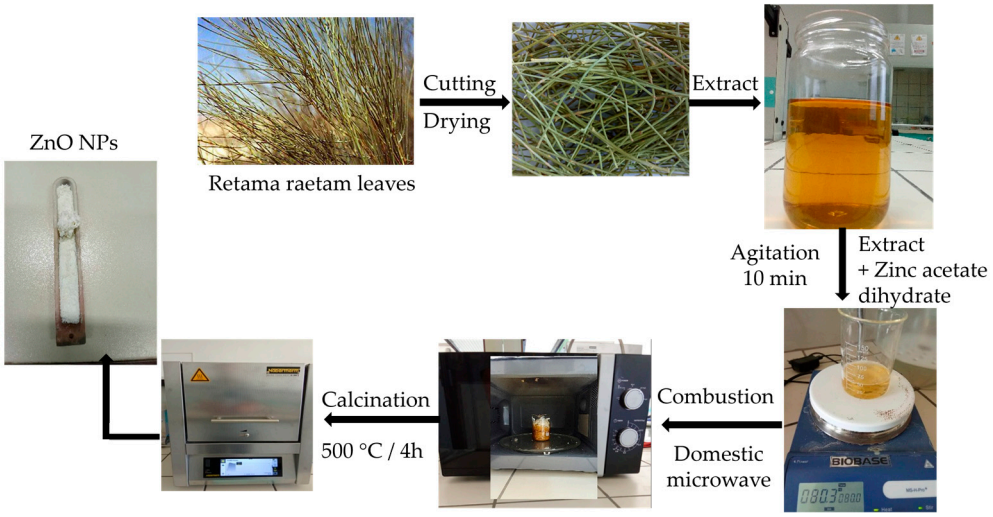


Figure 1. Schematic description of the green synthesis of ZnO NPs using the *R. raetam* leaf extract and zinc acetate dihydrate.

2.3. Sensor Fabrication and Sensing Tests

In 2.25 mL of DW, 250 mg of the synthesized nanopowder sample was dispersed, and the mixture was sonicated for 15 min in ultrasound to achieve a homogenous and well-dispersed solution. This homogeneous solution was subsequently deposited by spray coating onto alumina substrates (Al_2O_3). The sample substrate consisting of a pair of interdigitated gold electrodes (IDEs) and a platinum microheater (Figure 2a) was subjected to annealing in a muffle furnace set at 300 °C for 1 h in atmospheric air. This annealing step ensured the stability and adhesion of the deposited films. Detection tests were carried out using a custom-built gas detection measurement system. As shown in Figure 2b, the gas sensing performance was measured via continuous measurement of electrical resistance under air and the target gas conditions. The target gas (0.5, 1, 2.5, and 5 ppm) was introduced into the chamber for 10 min, followed by a 20 min purge with synthetic air. All tests were conducted under controlled conditions with 50% RH, maintained by bubbling the gas through DW.

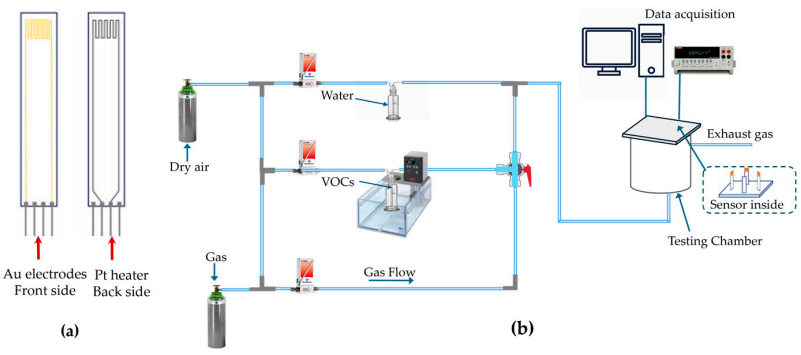


Figure 2. Schematic description of: (**a**) the sensor substrate and (**b**) the gas sensing system.

2.4. Characterization

Structural characterizations of the biosynthesized ZnO nanoparticles were performed on a Panalytical Empyrean diffractometer (Almelo, The Netherlands), with diffraction patterns acquired across a 2θ range of 17° to 75°. The morphological features of the synthesized ZnO NPs were examined using an S4800II Hitachi field emission scanning electron microscope (Waltham, MA, USA) coupled with energy dispersive X-ray analysis for elemental composition. The STEM analysis was conducted using the SEM-FEI Apreo S (Tokyo, Japan). In this instance, the micrographs were acquired at 30 kV, utilizing a copper–carbon grid as the sample holder, by employing bright-field imaging mode. Optical properties were assessed by obtaining UV-Vis absorbance spectra using a Shimadzu UV-3101PC spectrophotometer (Kyoto, Japan). Additionally, the functional groups present in both the *R. raetam* leaf extract and the biosynthesized ZnO NPs were analyzed using an FTIR spectrometer (PerkinElmer, Waltham, MA, USA). The Raman spectroscopy measurements were performed on a Horiba LabRAM HR (Kyoto, Japan) using a 532 nm laser.

3. Results and Discussion

3.1. X-Ray Analysis

The crystal structures of the biosynthesized nanoparticles (NPs) were examined through XRD. As shown in Figure 3, the diffraction pattern for ZnO exhibits distinct peaks, listed in Table 1, that are assigned to the hexagonal wurtzite structure of ZnO (JCPDS: 36-1451). The sharp and intense nature of the peaks indicates the high degree of crystallinity of the NPs. Additionally, the observed peak broadening in the XRD pattern suggests the presence of smaller crystallite sizes within the sample. The average sizes of ZnO NPs were determined by the Debye–Scherrer equation [31]:

$$D = \frac{k\lambda}{\beta \cos\theta} \quad (1)$$

where D refers to the dimension of the crystallites, K is the shape factor (generally 0.9), λ is the wavelength of the incoming X-rays, β is the FHWM, and θ is the angle of diffraction.

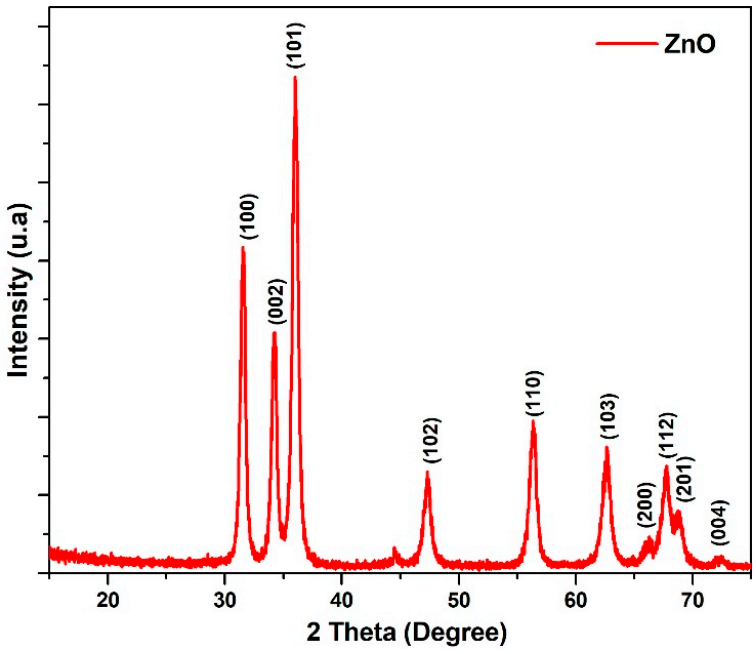


Figure 3. X-ray Diffractogram of the ZnO NPs.

Table 1. The particle size of the ZnO NPs was determined at various diffraction angles.

No. of Peaks	Miller Indices	2 Theta (°)	FWHM (°)	Particle Size (nm)
1	(100)	31.562	0.472	17.458
2	(002)	34.,234	0.509	16.321
3	(101)	36.033	0.541	15.430
4	(102)	47.321	0.641	13.529
5	(110)	56.356	0.636	14.149
6	(103)	62.640	0.740	12.558
7	(200)	66.336	0.994	9.539
8	(112)	67.727	0.710	13.471
9	(201)	68.815	0.682	14.100
Average size				14.062

The average crystallite size calculated for the ZnO NPs happens to be 14 nm, confirming their nano-scale dimensions (see Table 1). Additionally, the lattice parameters a and c were calculated from the diffraction peaks corresponding to the Miller indices (100) and (002) using the following relationships [32]:

$$a = \frac{\lambda}{\sqrt{3} sin\ \theta_{(100)}} \quad (2)$$

$$c = \frac{\lambda}{\sin \theta_{(002)}} \quad (3)$$

For the biosynthesized ZnO NPs, the lattice was determined to be a = b = 3.270 Å and c = 5.234 Å. The c/a ratio was found to be 1.6, consistent with an ideal close-packed hexagonal structure [33].

3.2. FTIR Spectroscopy

The FTIR spectroscopic technique is extensively utilized for the identification of biomolecules in plant extracts and inorganic materials [34]. These biomolecules act as reducing agents in the formation of NPs and are crucial for stabilizing the nanoparticles. Figure 4 presents the FTIR spectra of *R. raetam* and ZnO nanoparticles biosynthesized using *R. raetam*. The FTIR spectrum of the *R. raetam* leaf extract, as shown in Figure 4a, presents a number of well-defined peaks all over the range. Absorption peaks at 1229 cm^{-1}, 1365 cm^{-1}, 1449 cm^{-1}, 1634 cm^{-1}, 1726 cm^{-1}, 1738 cm^{-1}, 2155 cm^{-1}, 2855 cm^{-1}, 2970 cm^{-1}, and 3350 cm^{-1} were recorded. The 1229 cm^{-1} peak is due to stretching vibrations of C-N bonds in aliphatic and aromatic amines and stretching vibrations of C-O [35,36]. The marked peaks at 1365 cm^{-1} and 1449 cm^{-1} are those of an aromatic ring [37]. The absorption bands around 1634–1738 cm^{-1} are assigned to those of alkenes. Peaks observed at 2855 cm^{-1} and 2970 cm^{-1} account for stretching vibrations of C–H of alkanes [38]. A broad absorption near 3350 cm^{-1} was attributed to the stretching and bending vibrations of OH bonds in adsorbed water molecules [39]. The interactions between the phytomolecules existing in *R. raetam* and the surface of ZnO NPs are demonstrated in the FTIR spectra shown in Figure 4b. The spectra exhibit several intense peaks consistent with numerous functional groups of the *R. raetam* leaf extract, with minor shifts in peak positions and variations in intensity. Additionally, the FTIR spectrum of the ZnO nanoparticles reveals new peaks at 700 cm^{-1} and 600 cm^{-1}, which are associated with the stretching vibrations of the Zn-O bonds. The broad peak of the OH group was completely diminished after the formation of ZnO NPs. As a result, the FTIR results confirm that phenolic and flavonoid compounds obtained from the *R. raetam* plant extract are directly involved in reducing the precursors of zinc and stabilizing the subsequent ZnO nanoparticles.

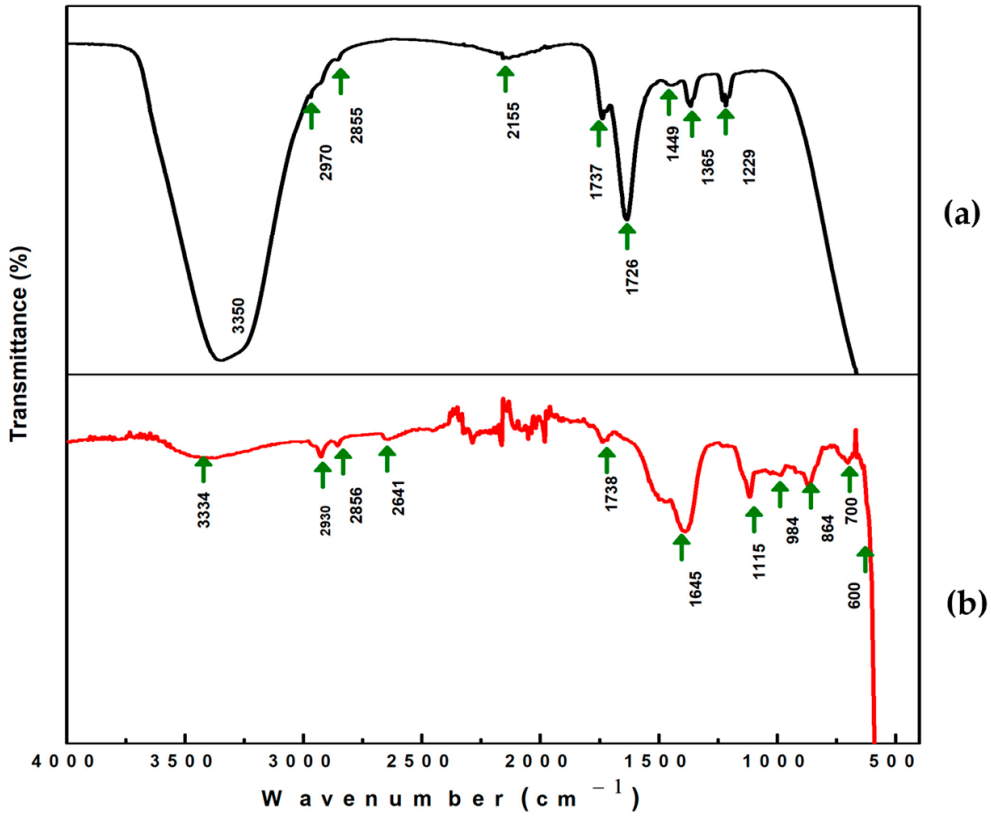


Figure 4. FTIR spectra of (**a**) *R. raetam* plant extract and (**b**) ZnO NPs.

3.3. FE-SEM and STEM Analysis

The morphology of the green-synthesized ZnO nanoparticles was analyzed using FE-SEM. As shown in Figure 5a, the ZnO NPs have a spherical shape and some agglomeration. The average particle size measured using ImageJ software (version 1.54p, Figure 5b) ranged from 10–50 nm while the mean diameter was approximately 24 nm. Meanwhile, the Debye–Scherrer equation calculated crystallite size lower than that obtained using SEM, because smaller nanoparticles tend to agglomerate to form larger ZnO NPs in the sample. According to EDS analysis (Figure 5c), zinc (Zn) and oxygen (O) are present as the main elements with weight percentages of 55.6% and 18.5%, respectively. Other elements such as carbon, magnesium, aluminum, calcium and potassium were detected at 23.5, 0.2, 1.7, 0.2, and 0.3 weight percentages, respectively, suggesting the possible presence of organic materials acting as capping agents during the synthesis process such as proteins, amino acids, sugars, and polysaccharides as a result of X-ray emissions [40,41].

The high magnification of the STEM images (Figure 5d) was used to characterize the size and shape of the biosynthesized ZnO NPs. The NPs have been recorded in various morphologies including spherical and hexagonal shapes. Notably, the spherical NPs were found to have a more homogeneous size distribution, averaging approximately 27 nm in particle size. As summarized in the comparative table (Supplementary Table S1), green-synthesized ZnO nanoparticles reported in the literature generally display diverse morphologies and a broad particle size distribution, typically ranging from 20 to 60 nm. In contrast, the ZnO nanoparticles synthesized in the present work exhibit a predominantly spherical morphology with a narrow size distribution of 24–27 nm, which is particularly advantageous for gas sensing applications.

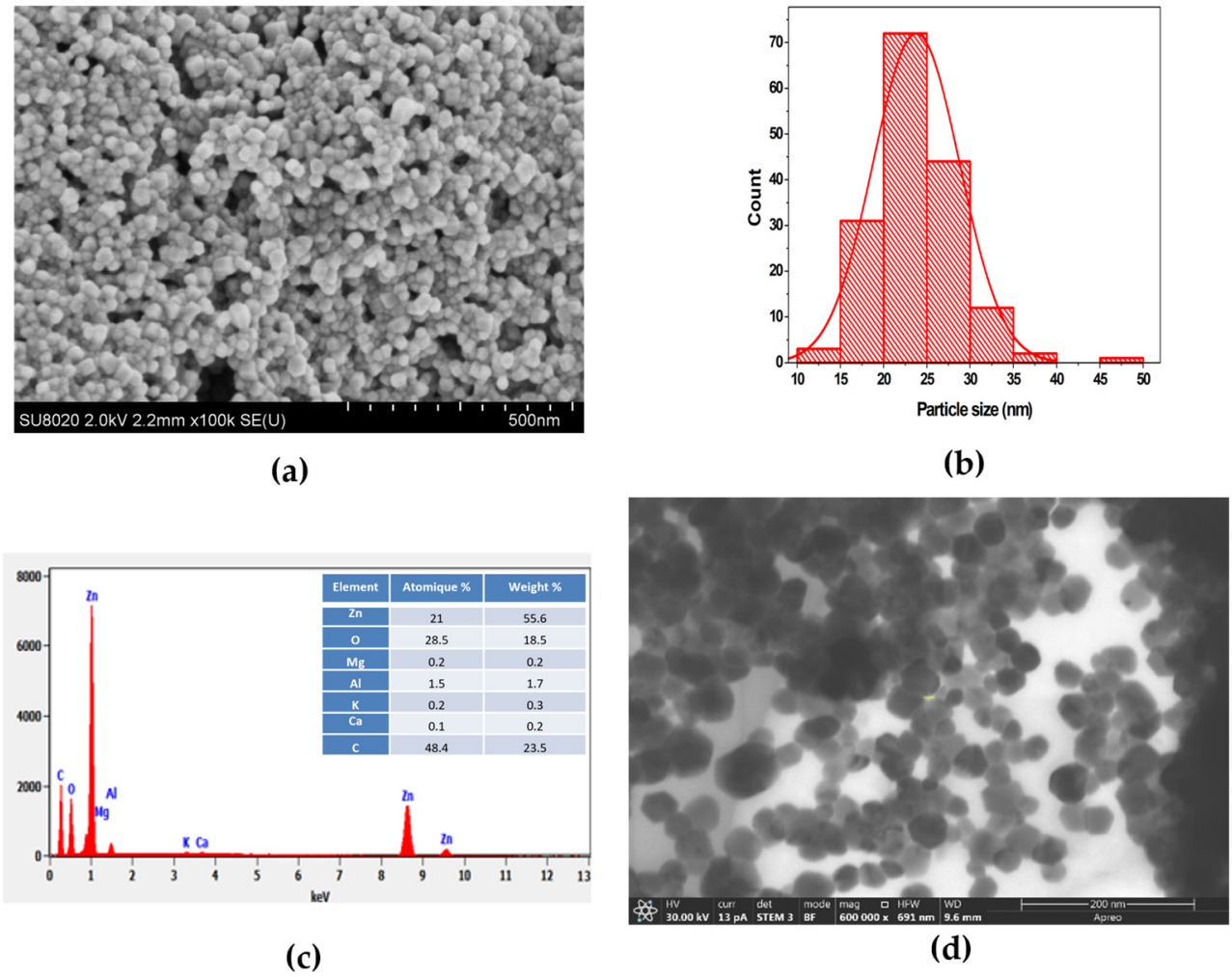


Figure 5. (**a**) SEM analysis, (**b**) histogram depicting the particle size distribution derived from SEM images, (**c**) EDS spectrum, and (**d**) STEM images of biosynthesized ZnO NPs.

3.4. UV-Vis Spectroscopy

Optical characterization was performed by measuring the diffuse reflectance of the samples at ambient temperature. Figure 6 displays the typical reflectance spectra of the ZnO samples, showing a strong absorption edge from 200–800 nm. UV–visible reflectance spectroscopy is a mechanistic technique that can be employed widely to determine material band gaps. The diffuse reflectance sample (R) was analyzed by the Kubelka–Munk function, F(R), which is expressed as [42,43]:

$$F(R) = \frac{(1 - R)^2}{2R} \quad (4)$$

where R represents the absolute reflectance value. The bandgap energy of the ZnO NPs was determined by extrapolating the linear portion of the plot of $[F(R)hv]^2$ versus photon energy (in eV) to F(R) = 0; the resulting intercept corresponds to the direct band gap energy. The inset in Figure 6 illustrates the calculation of the band edge using the Kubelka–Munk function for the ZnO sample. The calculated band edge value for the ZnO NPs was found to be 3.23 eV.

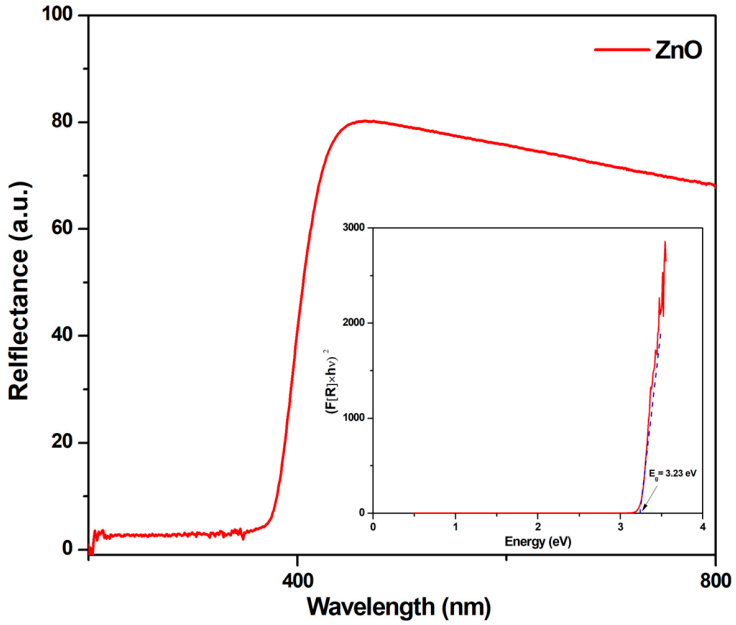


Figure 6. Reflectance spectra of ZnO NPs as a function of wavelength. The inset is an illustration of an estimation of band gap energy of the ZnO NPs by the K-Munk function. The blue line corresponds to the extrapolation of the linear region of the versus photon energy (eV) plot.

3.5. Raman Spectroscopy

Raman spectroscopy is a powerful tool for examination of microstructures and nanostructures, providing information about their crystallization and structural disorder, as well as defects. The Raman spectrum (Figure 7) shows several phonon modes typical of hexagonal wurtzite ZnO. These peaks represent the observed modes at 96 cm^{-1} for E_{2L} and 433 cm^{-1} and 580 cm^{-1} for E_{2H} and A_1(LO), respectively. The sharp and prominent E_{2H} mode is a key indicator of the crystalline wurtzite structure. Furthermore, the peak at 328 cm^{-1} comes from E_{2H}–E_{2L} multiphonon scattering [44]. The A_1(LO) mode is frequently associated with crystal defects, thus suggesting the presence of either oxygen vacancies or zinc interstitials [45].

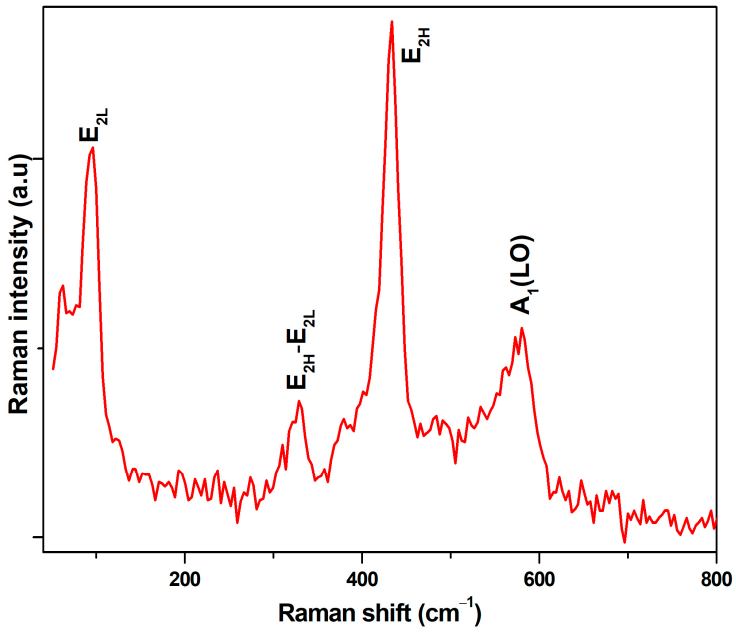


Figure 7. Raman Spectrum of ZnO NPs.

3.6. Gas Sensing Studies

In Figure 8a, the initial resistance of the sensor in air decreases with increasing temperature. This behavior indicates semiconductor properties, where the electrons gain more energy at high temperatures to transfer from the valence band of ZnO to the conduction band, thus reducing the resistance.

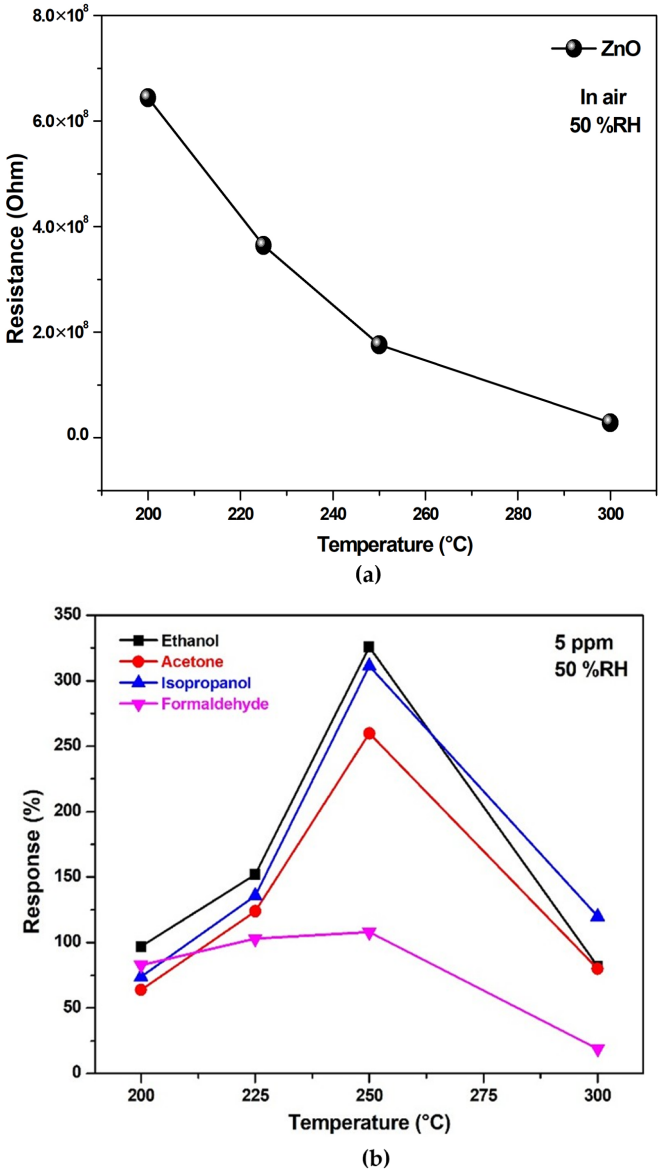


Figure 8. (**a**) Temperature-dependent variation of the base resistance of the ZnO biosynthesized gas sensor measured in air, and (**b**) Sensor response of the ZnO biosynthesized gas sensor with respect to 5 ppm of acetone, ethanol, isopropanol, and formaldehyde at different operation temperatures at 50% RH.

The response (S) of the sensor is expressed as follows:

$$S\ (\%) = \frac{R_a - R_g}{R_g} \times 100 \quad (5)$$

where Rg and Ra are the electrical resistances of ZnO measured in the presence of target reducing gas and air, respectively.

Therefore, the ZnO-NP-based sensors were tested with four different VOCs, ethanol, acetone, formaldehyde, and isopropanol, at a concentration of 5 ppm and 50% RH to

determine their optimal operating temperature. The measurements were carried out over a temperature range of 200–300 °C. The temperature at which the sensors exhibited maximum sensitivity to these gases is defined as the optimal operating point. Maximum responses (Figure 8b) were observed at an operating temperature of 250 °C, which is the best for sensor performance. At this temperature, the ZnO-based sensor revealed a greater response to ethanol than to acetone, isopropanol, and formaldehyde gases.

The dynamic resistance responses of ZnO-based gas sensors to ethanol, isopropanol, acetone, and formaldehyde are shown in Figure 9a–d. These results demonstrate that the developed sensors can detect low concentrations of tested VOCs, with performance varying depending on the specific gas. Upon exposure to each gas, the resistance of the sensor decreases, confirming its n-type semiconductor characteristics. Then, electrical resistance returns to its baseline after the VOC is released, demonstrating the excellent reversibility of the ZnO-based sensor's response.

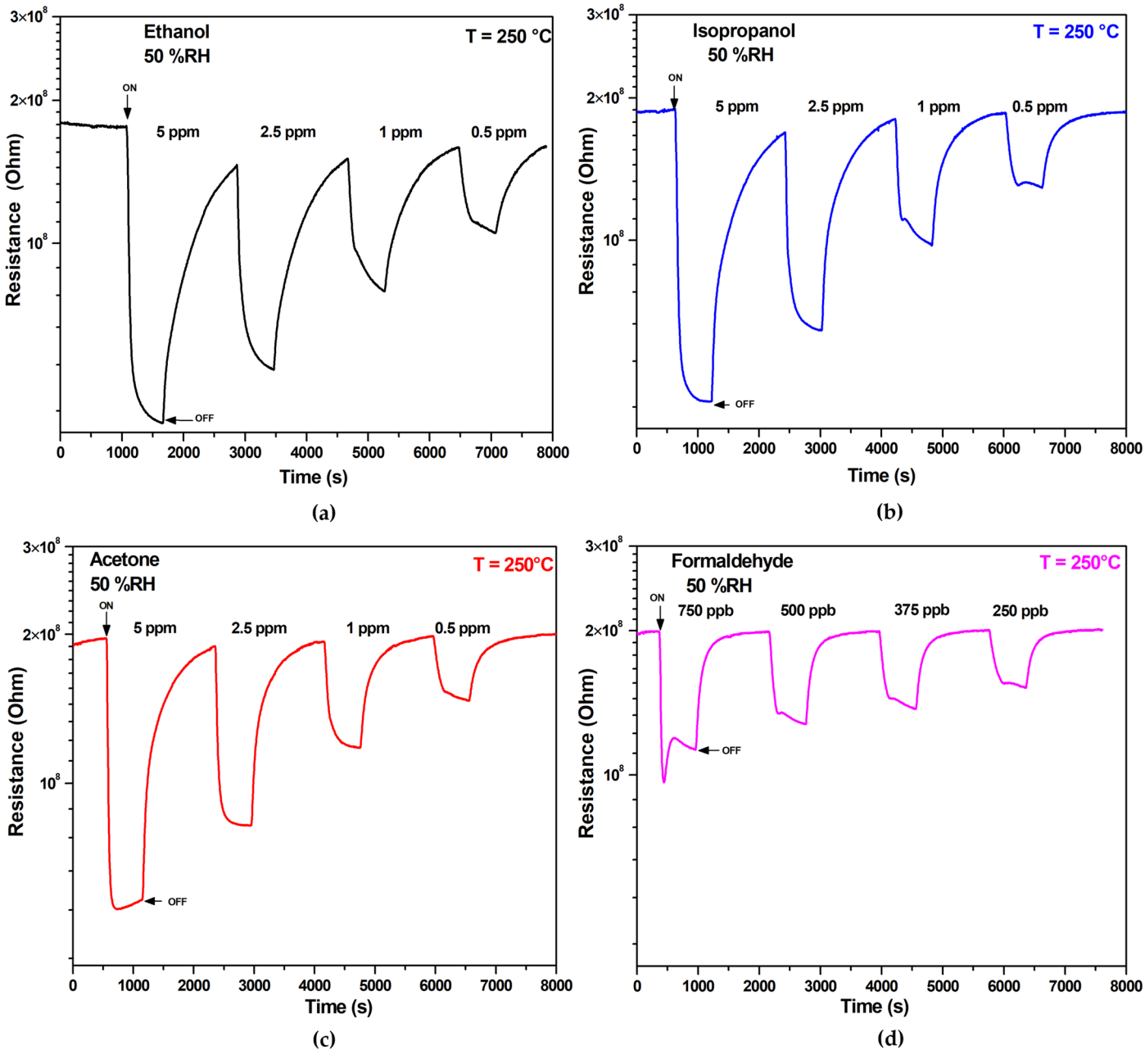


Figure 9. Transient response of ZnO sensor working at 250 °C under different concentrations of (**a**) ethanol, (**b**) isopropanol, (**c**) acetone and (**d**) formaldehyde.

As shown in Figure 10, the ZnO sensor exhibits a linear response to increasing VOC concentrations under operating conditions of 250 °C and 50% RH. Furthermore, its sensing response to ethanol is much more pronounced than those for other tested VOCs. Specifically, the sensor demonstrated responses of 69%, 124%, 229%, and 325% to ethanol concentrations of 0.5, 1, 2.5, and 5 ppm, respectively. These results highlight the sensor's strong and consistent responsiveness to ethanol across a range of concentrations.

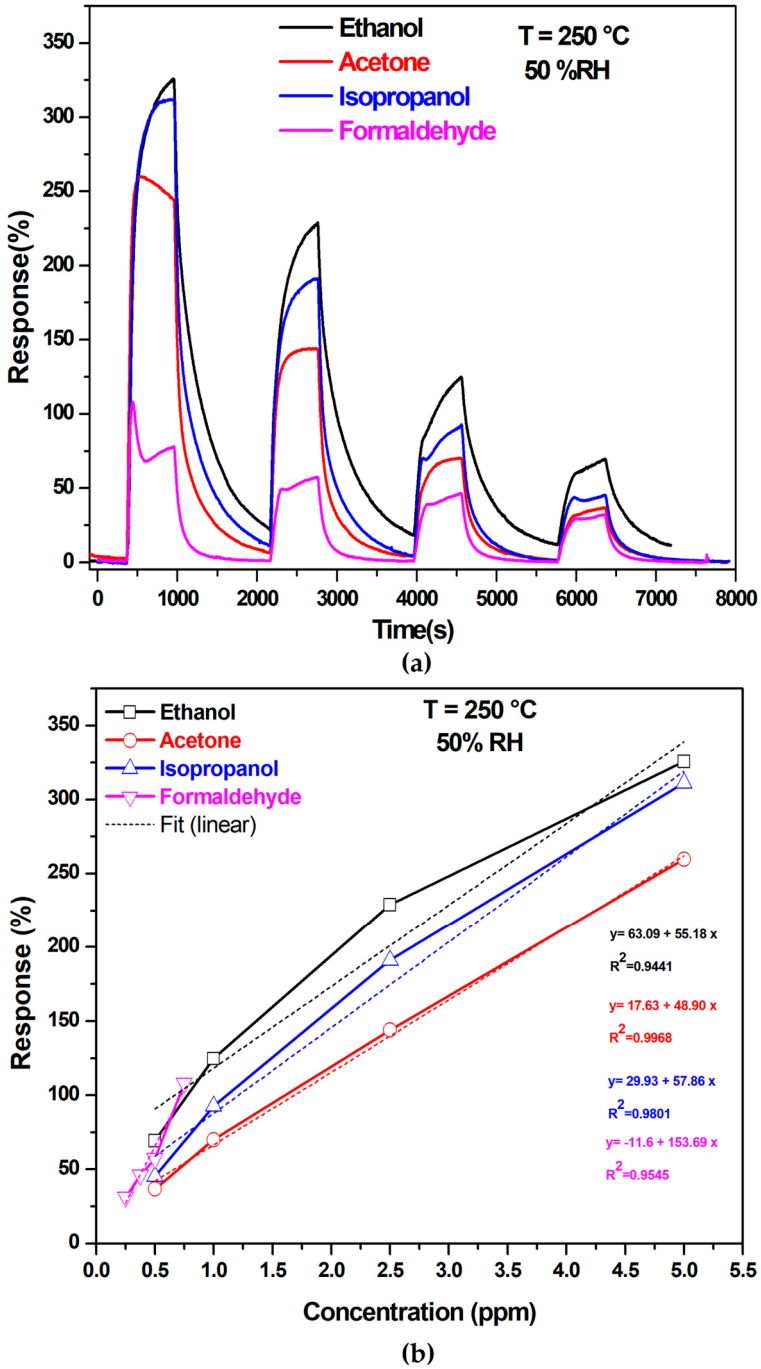


Figure 10. (**a**) Response of ZnO sensor toward various gas concentrations of ethanol, acetone, isopropanol, and formaldehyde at 250 °C and (**b**) Linear fit to the data.

The sensitivity of the developed selective ZnO-based ethanol sensor, defined as the slope of the calibration curve, is 55.18 ppm^{-1}.

Figure 11 illustrates the responses of the ZnO-based gas sensor to 500 ppb of ethanol, isopropanol, acetone, and formaldehyde gas at 50% RH and a temperature of 250 °C.

As evident from the results, the ZnO sensor exhibits a significantly higher response to ethanol compared to the other tested gases, highlighting its excellent selectivity for ethanol detection.

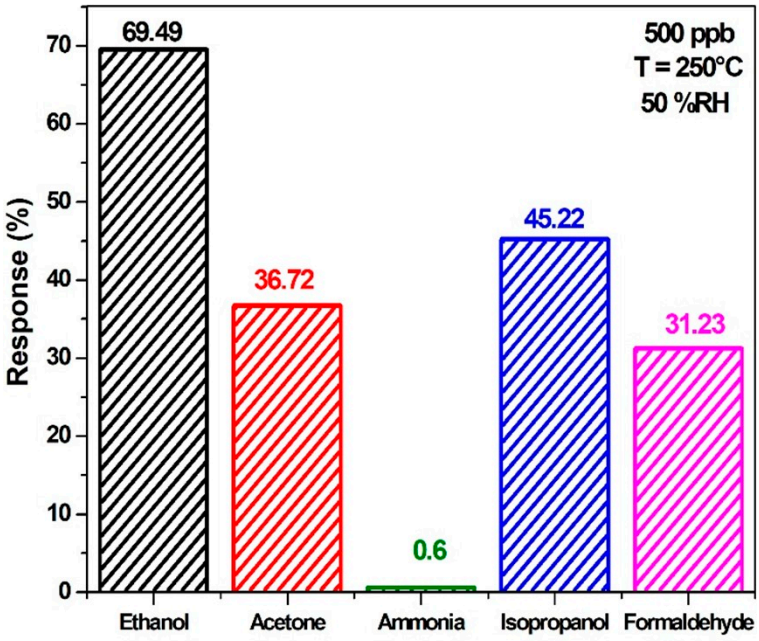


Figure 11. Selectivity of ZnO-based sensor for 500 ppb of different target gases such as ethanol, acetone, isopropanol, ammonia and formaldehyde at 250 °C and 50% RH.

The limit of detection (LOD) is considered to be that concentration at which the response of the sensor can be distinguished prominently from that of the noise signal. It is usually expressed as threefold standard deviation of the noise.

The sensor's noise level was determined first by evaluating the transduction response under baseline conditions before exposure to ethanol. The noise was quantified by taking an average signal of ten consecutive baseline measurements and calculating the root mean square deviation (RMSD) using the following equation [46]:

$$RMSD = \sqrt{\frac{\sum_1^N (S - S_i)^2}{N}} \quad (6)$$

where N represents the sequence of measurements at time points, Si refers to the measurement response of the baseline reading. The determination of the LOD is performed using the following equation:

$$LOD = \frac{3.RMSD}{Sensitivity} \quad (7)$$

The ZnO-based sensor can detect ethanol at concentrations as low as 3.92 ppb, enabling the early identification of ethanol leaks. In addition, the sensor exhibits low detection limits of 5.56 ppb for acetone, 7.15 ppb for isopropanol, and 2.45 ppb for formaldehyde.

The response time of the sensor, defined as the time to reach 90% of the total resistance change, is 94 s. On the other hand, recovery time takes approximately 981 s, which is very long. Thus, the response time can be effective for ethanol detection, while the long recovery time indicates that ethanol is desorbing from the sensor surface at a slower rate. The response and recovery time differences could be attributed to the intense interaction of ethanol molecules with the ZnO NPs.

Figure 12 shows the repeatability of the ZnO-based gas sensor tested for seven cycles of exposure to 5 ppm ethanol gas at 250 °C. The sensing curves appear highly similar,

with repeated response values, demonstrating a good repeatability and reliability of the developed gas sensor.

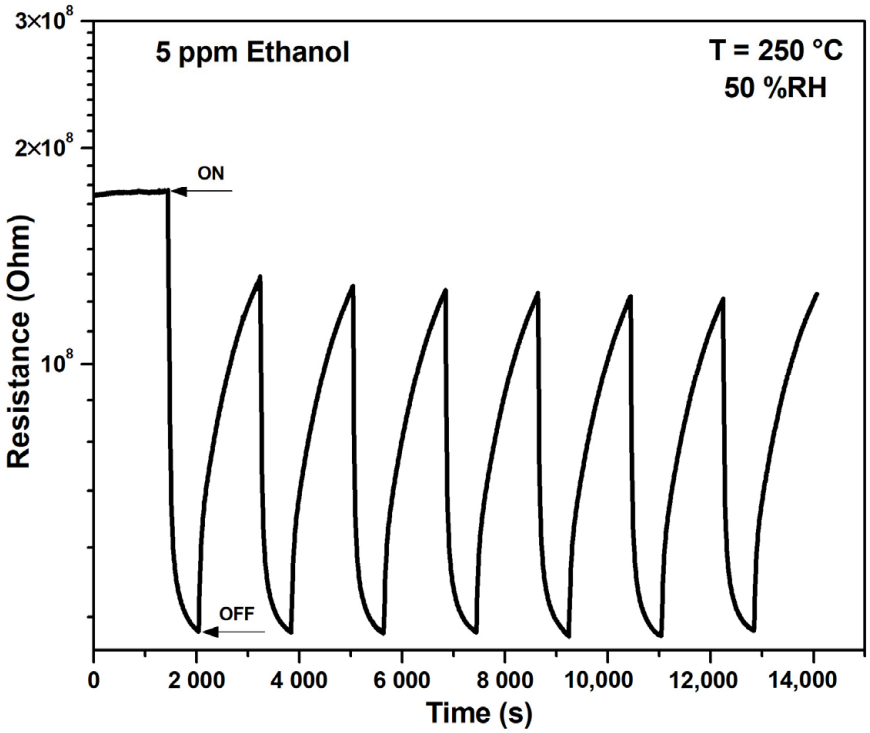


Figure 12. Reproducibility tests of ethanol sensor (5 ppm concentration) at 250 °C.

Figure 13a shows the dynamic resistance responses of the developed ZnO-based gas sensor to 5 ppm of ethanol gas under different humidity levels of 10%, 30%, 50%, 70%, and 90%. The sensor's resistance fell rapidly at first with the increasing humidity and then started to rise exponentially. The baseline resistance of the sensor stayed relatively constant from 30–90% RH, with little fluctuation (less than 24%) in response to changes in humidity (Figure 13b).

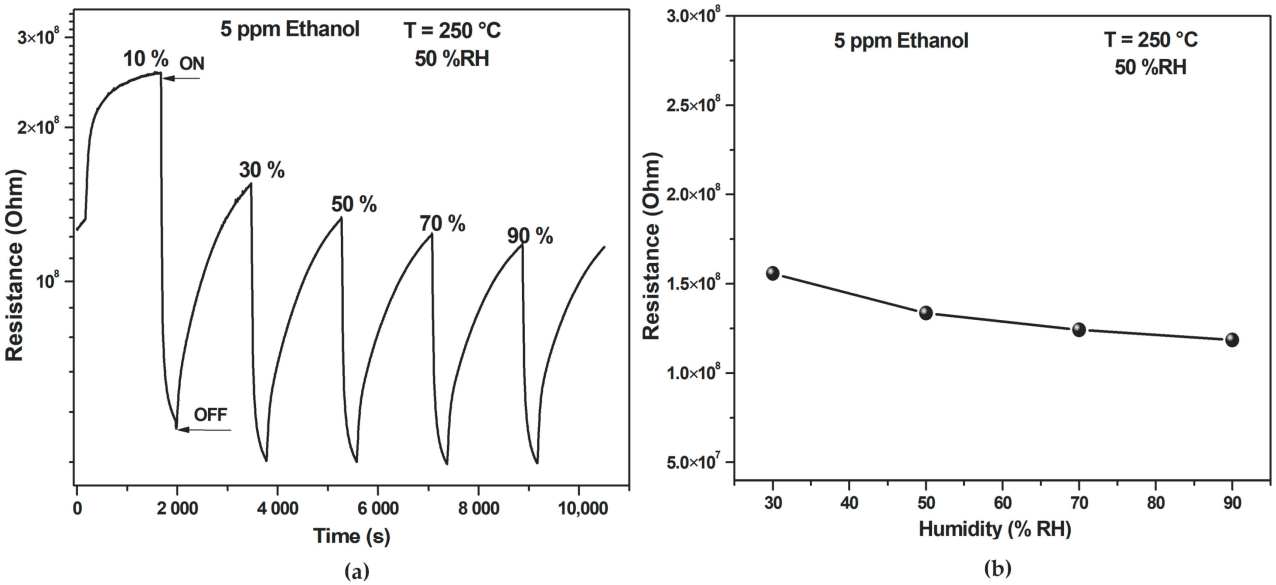


Figure 13. (**a**) Dynamic response of ZnO-based sensor at different RH levels (10–90%) and (**b**) Resistance as function of RH.

This behavior is due to the adsorption of water molecules on the sensor's surface, which, at low humidity levels, enhances conductivity and reduces resistance. After that, with increasing humidity, a thick layer of water would act on the interaction of the ethanol gas with the sensor, thus resulting in reduced response and exponential resistance increase. These observations mean that the sensor responds to humidity changes with reasonably stable electrical properties and repeatable characteristics. Using ZnO nanoparticles, the sensor is reliable for gas sensing, even when humidity varies. The sensing performance of the sensor for VOCs developed in this work has been compared with that of results reported earlier (Table 2). The results show that the sensor fabricated using ZnO NPs shows better response. The sensor detects VOCs at a concentration as low as 5 ppm with a high response value at around 325%. This result indicates the superior sensing capability of the biosynthesized ZnO NPs compared to materials reported earlier, highlighting their excellent promise as a candidate for use in sensor applications.

Table 2. Ethanol gas responses of ZnO-based sensors: Literature vs. Current Findings.

Materials	Detection Range (ppm)	Synthesis Method	Working Temperature (°C)	Gas Response	Refs
ZnO/Au NPs	20–100	Hydrothermal	270	86.9 [a]	[47]
ZnO NSs	50–1000	Aqueous solution	270	2.27 [b]	[48]
ZnO/CuO	100–500	Co-precipitation	300	228 [a]	[49]
Ag-ZnO	50–3000	Biosynthesis	250	30.55 [a]	[50]
ZnO NPs	25–100	Co-precipitation	250	51.13 [a]	[51]
ZnO NPs without IC	40–800	Precipitation	285	3.97 [b]	[52]
CuO nanoplates	10–100	Hydrothermal	250	176 [a]	[53]
NiO/ZnO	5–50	Vapor–liquid–solid	400	6.7 [c]	[54]
NiO/ZnO	10–800	Atomic layer deposition	400	2.88 [b]	[55]
NiO	50–1000	Nanocasting	300	2.18 [a]	[56]
ZnO NPs	0.5–5	Green microwave-assisted combustion	250	325 [a]	This work

[a]: response (%) = $\Delta R/R \times 100$, [b]: response = Ra/Rg, [c]: response (%) $\Delta G/G \times 100$.

3.7. Gas Sensing Mechanism

The gas sensing mechanism for ZnO nanoparticles depends on the electrical resistance of the sensing material. After the adsorption of the oxygen molecules from the atmosphere onto the ZnO surface, these molecules take electrons from the material's conduction band, forming oxygen like ions O_2^- and O^-. When a reducing gas is introduced onto the surface, it interacts with the surface ions and releases the trapped electrons back into the conduction band. Hence, the increase in charge carrier concentration will lead to a decrease in the electrical resistance of the material, which can be measured.

Ethanol, as a small polar molecule containing a hydroxyl (–OH) group, can strongly interact with surface-adsorbed oxygen species and active sites on the ZnO sensor through hydrogen bonding and dipole–dipole interactions. These interactions enhance adsorption efficiency and facilitate rapid surface oxidation, causing a pronounced release of electrons into the conduction band and a significant change in electrical resistance.

4. Conclusions

In this study, we developed a simple, low-cost and environmentally friendly green method for producing ZnO NPs using a plant extract from *R. raetam*. FTIR analysis showed that functional groups of *R. raetam* play a crucial role in the synthesis and stabilization of ZnO NPs. The nanoparticles, characterized by SEM and STEM imaging, presented a hexagonal wurtzite structure and were obtained in a high degree of purity and with an average crystallite size of about 14 nm. Spectroscopic analysis indicated strong UV absorption, with an estimated band gap energy of 3.23 eV. Gas sensing studies indicated that the ZnO-based sensor has excellent response and reproducibility with low concentrations of VOCs, particularly ethanol, under optimal conditions of 250 °C and 50% RH. The sensor demonstrated good stability under varying humidity levels, and the detection limit was below 4 ppb. These results present potential uses for the green-synthesized ZnO nanoparticles in rapid and reliable monitoring of IAQ.

Supplementary Materials: The following supporting information can be downloaded at: https://www.mdpi.com/article/10.3390/chemosensors14020042/s1, Table S1: Comparative summary of ZnO properties.

Author Contributions: Conceptualization, T.S., M.E., C.D. and D.L.; methodology, T.S., M.E., C.D. and D.L.; software, A.L. and M.D.; validation, C.D., D.L. and M.D.; formal analysis, M.D.; investigation, M.E. and A.L.; resources, C.D., M.D. and D.L.; data curation, T.S., M.D. and D.L.; writing—original draft preparation, T.S. and A.L.; writing—review and editing, C.D. and D.L.; visualization, D.L.; supervision, C.D. and D.L.; project administration, C.D. and D.L.; funding acquisition, T.S., C.D. and D.L. All authors have read and agreed to the published version of the manuscript.

Funding: This work was supported by the NANO-2ECO project (21PEJC D1P11) under the Young Researchers Encouragement Program PEJC 2021, funded by the Tunisian Ministry of Higher Education and Scientific Research. It was also financially supported by the European Regional Development Fund (ERFD) and the Walloon Region of Belgium through the INTERREG VI FWVL (France-Wallonie-Vlaanderen) Program, under ALCOVE (N°.0100143) and CleanAirBouw (N°.0100179) projects.

Institutional Review Board Statement: Not applicable.

Informed Consent Statement: Not applicable.

Data Availability Statement: Dataset available on request from the authors.

Conflicts of Interest: The authors declare no conflicts of interest.

References

1. Mirzaei, A.; Leonardi, S.G.; Neri, G. Detection of hazardous volatile organic compounds (VOCs) by metal oxide nanostructures-based gas sensors: A review. *Ceram. Int.* **2016**, *42*, 15119–15141. [CrossRef]
2. You, B.; Zhou, W.; Li, J.; Li, Z.; Sun, Y. A review of indoor Gaseous organic compounds and human chemical Exposure: Insights from Real-time measurements. *Environ. Int.* **2022**, *170*, 107611. [CrossRef]
3. Bhat, A.A.; Afzal, M.; Goyal, A.; Gupta, G.; Thapa, R.; Almalki, W.H.; Kazmi, I.; Alzarea, S.I.; Shahwan, M.; Paudel, K.R.; et al. The impact of formaldehyde exposure on lung inflammatory disorders: Insights into asthma, bronchitis, and pulmonary fibrosis. *Chem. Biol. Interact.* **2024**, *394*, 111002. [CrossRef] [PubMed]
4. Vardoulakis, S.; Giagloglou, E.; Steinle, S.; Davis, A.; Sleeuwenhoek, A.; Galea, K.S.; Dixon, K.; Crawford, J.O. Indoor exposure to selected air pollutants in the home environment: A systematic review. *Int. J. Environ. Res. Public Health* **2020**, *17*, 8972. [CrossRef]
5. Mirzaei, A.; Ansari, H.R.; Shahbaz, M.; Kim, J.Y.; Kim, H.W.; Kim, S.S. Metal Oxide Semiconductor Nanostructure Gas Sensors with Different Morphologies. *Chemosensors* **2022**, *10*, 289. [CrossRef]
6. Waqas Alam, M.; Sharma, A.; Sharma, A.; Kumar, S.; Mohammad Junaid, P.; Awad, M. VOC Detection with Zinc Oxide Gas Sensors: A Review of Fabrication, Performance, and Emerging Applications. *Electroanalysis* **2025**, *37*, e202400246. [CrossRef]
7. Bhati, V.S.; Hojamberdiev, M.; Kumar, M. Enhanced sensing performance of ZnO nanostructures-based gas sensors: A review. *Energy Rep.* **2020**, *6*, 46–62. [CrossRef]

8. Ferlazzo, A.; Neri, G.; Donato, A.; Gugliandolo, G.; Latino, M. Room Temperature NO_2-Sensing Properties of N-Doped ZnO Nanoparticles Activated by UV-Vis Light. *Sensors* **2025**, *25*, 114.
9. Luo, Y.; Ly, A.; Lahem, D.; Zhang, C.; Debliquy, M. A novel low-concentration isopropanol gas sensor based on Fe-doped ZnO nanoneedles and its gas sensing mechanism. *J. Mater. Sci.* **2021**, *56*, 3230–3245. [CrossRef]
10. Du, W.; Feng, K.; Li, C.; Li, S.; Abidin, Z.U.; Yin, H.; Chen, S. Controlled synthesis of zinc oxide nanoparticles through flame spray pyrolysis and evaluation of their anticancer effects against gastric cancer cell. *Arab. J. Chem.* **2023**, *16*, 105192. [CrossRef]
11. Porrawatkul, P.; Pimsen, R.; Kuyyogsuy, A.; Teppaya, N.; Noypha, A.; Chanthai, S.; Nuengmatcha, P. Microwave-assisted synthesis of Ag/ZnO nanoparticles using Averrhoa carambola fruit extract as the reducing agent and their application in cotton fabrics with antibacterial and UV-protection properties. *RSC Adv.* **2022**, *12*, 15008–15019. [CrossRef]
12. Wojnarowicz, J.; Chudoba, T.; Lojkowski, W. A review of microwave synthesis of zinc oxide nanomaterials: Reactants, process parameters and morphoslogies. *Nanomaterials* **2020**, *10*, 1086. [CrossRef]
13. Dadkhah, M.; Tulliani, J.M. Green Synthesis of Metal Oxides Semiconductors for Gas Sensing Applications. *Sensors* **2022**, *22*, 4669. [CrossRef]
14. Sadhasivam, S.; Shanmugam, M.; Umamaheswaran, P.D.; Venkattappan, A.; Shanmugam, A. Zinc Oxide Nanoparticles: Green Synthesis and Biomedical Applications. *J. Clust. Sci.* **2021**, *32*, 1441–1455. [CrossRef]
15. Nandhini, J.; Karthikeyan, E.; Rajeshkumar, S. Green Synthesis of Zinc Oxide Nanoparticles: Eco-Friendly Advancements for Biomedical Marvels. *Resour. Chem. Mater.* **2024**, *3*, 294–316. [CrossRef]
16. El-Saadony, M.T.; Fang, G.; Yan, S.; Alkafaas, S.S.; El Nasharty, M.A.; Khedr, S.A.; Hussien, A.M.; Ghosh, S.; Dladla, M.; Elkafas, S.S.; et al. Green Synthesis of Zinc Oxide Nanoparticles: Preparation, Characterization, and Biomedical Applications—A Review. *Int. J. Nanomed.* **2024**, *19*, 12889–12937. [CrossRef]
17. Barzinjy, A.A.; Azeez, H.H. Green synthesis and characterization of zinc oxide nanoparticles using *Eucalyptus globulus* Labill. leaf extract and zinc nitrate hexahydrate salt. *SN Appl. Sci.* **2020**, *2*, 991. [CrossRef]
18. Iqbal, J.; Abbasi, B.A.; Yaseen, T.; Zahra, S.A.; Shahbaz, A.; Shah, S.A.; Uddin, S.; Ma, X.; Raouf, B.; Kanwal, S.; et al. Green synthesis of zinc oxide nanoparticles using *Elaeagnus angustifolia* L. leaf extracts and their multiple in vitro biological applications. *Sci. Rep.* **2021**, *11*, 20988. [CrossRef]
19. Meji, A.A.; Usha, D.; Ashwin, B.M. Microwave-assisted green synthesis of zinc oxide nanoparticles using pistia stratiotes for anticancer and antibacterial applications. *Mater. Res. Express* **2024**, *11*, 085004. [CrossRef]
20. Ashwini, J.; Aswathy, T.R.; Rahul, A.B.; Thara, G.M.; Nair, A.S. Synthesis and characterization of zinc oxide nanoparticles using acacia caesia bark extract and its photocatalytic and antimicrobial activities. *Catalysts* **2021**, *11*, 1507. [CrossRef]
21. El Golli, A.; Fendrich, M.; Bazzanella, N.; Dridi, C.; Miotello, A.; Orlandi, M. Wastewater remediation with ZnO photocatalysts: Green synthesis and solar concentration as an economically and environmentally viable route to application. *J. Environ. Manag.* **2021**, *286*, 112226. [CrossRef]
22. El Golli, A.; Contreras, S.; Dridi, C. Bio-synthesized ZnO nanoparticles and sunlight-driven photocatalysis for environmentally-friendly and sustainable route of synthetic petroleum refinery wastewater treatment. *Sci. Rep.* **2023**, *13*, 20809.
23. Jayachandran, A.; Aswathy, T.R.; Nair, A.S. Green synthesis and characterization of zinc oxide nanoparticles using Cayratia pedata leaf extract. *Biochem. Biophys. Rep.* **2021**, *26*, 100995. [CrossRef] [PubMed]
24. Dinga, E.; Mthiyane, D.M.N.; Marume, U.; Botha, T.L.; Horn, S.; Pieters, R.; Wepener, V.; Ekennia, A.; Onwudiwe, D.C. Biosynthesis of ZnO nanoparticles using Melia azedarach seed extract: Evaluation of the cytotoxic and antimicrobial potency. *OpenNano* **2022**, *8*, 100068. [CrossRef]
25. Benzarti, Z.; Neiva, J.; Faia, P.; Silva, E.; Carvalho, S.; Devesa, S. Novel Green Synthesis Route of ZnO Nanoparticles for Dielectric Applications. *Nanomaterials* **2025**, *15*, 991. [CrossRef]
26. Elsamra, R.M.I.; Masoud, M.S.; Zidan, A.A.; Zokm, G.M.E.; Okbah, M.A. Green synthesis of nanostructured zinc oxide by Ocimum tenuiflorum extract: Characterization, adsorption modeling, cytotoxic screening, and metal ions adsorption applications. *Biomass Convers. Biorefinery* **2024**, *14*, 16843–16856.
27. Saada, M.; Wasli, H.; Jallali, I.; Kboubi, R.; Girard-lalancette, K.; Mshvildadze, V.; Ksouri, R.; Legault, J.; Cardoso, S.M. Bio-guided fractionation of retama raetam (Forssk.) webb & berthel polar extracts. *Molecules* **2021**, *26*, 5800. [CrossRef]
28. Mariem, S.; Hanen, F.; Inès, J.; Mejdi, S.; Riadh, K. Phenolic profile, biological activities and fraction analysis of the medicinal halophyte Retama raetam. *Afr. J. Bot.* **2014**, *94*, 114–121. [CrossRef]
29. Alfalluos, K.A.; Alnade, H.S.; Kollab, W.A.; Alafid, F.; Edrah, M.S. Qualitative and Quantitative phytochemical Analysis and Antimicrobial Activity of "Retama" Extract Grown in Zliten Libya. *Int. J. Med. Sci. Clin. Invent.* **2017**, *4*, 2861–2866. [CrossRef]
30. Rejab, A.; Ksibi, H. Phenolic and Flavonoid Contents of Some Plant Extracts from Tunisia Southern Landscape by Using Different Extraction Techniques: The Case of Retama reatam. *Med. Aromat. Plants* **2019**, *8*, 337. [CrossRef]
31. Rajan, M.; Anthuvan, A.J.; Muniyandi, K.; Kalagatur, N.K.; Shanmugam, S.; Sathyanarayanan, S.; Chinnuswamy, V.; Thangaraj, P.; Narain, N. Comparative Study of Biological (*Phoenix loureiroi* Fruit) and Chemical Synthesis of Chitosan-Encapsulated Zinc Oxide Nanoparticles and their Biological Properties. *Arab. J. Sci. Eng.* **2020**, *45*, 15–28. [CrossRef]

32. Dhahri, R.; Benamara, M.; Nassar, K.I.; Elkenany, E.B.; Al-Syadi, A.M. Zinc oxide-based sensor prepared by modified sol-gel route for detection of low concentrations of ethanol, methanol, acetone, and formaldehyde. *Semicond. Sci. Technol.* **2024**, *39*, 115021. [CrossRef]
33. Singhal, S.; Kaur, J.; Namgyal, T.; Sharma, R. Cu-doped ZnO nanoparticles: Synthesis, structural and electrical properties. *Phys. B Condens. Matter* **2012**, *407*, 1223–1226.
34. Karam, S.T.; Abdulrahman, A.F. Green Synthesis and Characterization of ZnO Nanoparticles by Using Thyme Plant Leaf Extract. *Photonics* **2022**, *9*, 594. [CrossRef]
35. Ghidan, A.Y.; Al-Antary, T.M.; Salem, N.M.; Awwad, A.M. Facile Green Synthetic Route to the Zinc Oxide (ZnONPs) Nanoparticles: Effect on Green Peach Aphid and Antibacterial Activity. *J. Agric. Sci.* **2017**, *9*, 131. [CrossRef]
36. Meer, B.; Andleeb, A.; Iqbal, J.; Ashraf, H.; Meer, K.; Ali, J.S.; Drouet, S.; Anjum, S.; Mehmood, A.; Khan, T.; et al. Bio-Assisted Synthesis and Characterization of Zinc Oxide Nanoparticles from *Lepidium sativum* and Their Potent Antioxidant, Antibacterial and Anticancer Activities. *Biomolecules* **2022**, *12*, 855. [CrossRef]
37. Tilahun, E.; Adimasu, Y.; Dessie, Y. Biosynthesis and Optimization of ZnO Nanoparticles Using *Ocimum lamifolium* Leaf Extract for Electrochemical Sensor and Antibacterial Activity. *ACS Omega* **2023**, *8*, 27344–27354. [CrossRef]
38. Muhaymin, A.; Mohamed, H.E.A.; Hkiri, K.; Safdar, A.; Azizi, S.; Maaza, M. Green synthesis of magnesium oxide nanoparticles using Hyphaene thebaica extract and their photocatalytic activities. *Sci. Rep.* **2024**, *14*, 20135. [CrossRef]
39. Almarhoon, Z.M.; Indumathi, T.; Kumar, E.R. Optimized green synthesis of ZnO nanoparticles: Evaluation of structural, morphological, vibrational and optical properties. *J. Mater. Sci. Mater. Electron.* **2022**, *33*, 23659–23672. [CrossRef]
40. El-Belely, E.F.; Farag, M.M.S.; Said, H.A.; Amin, A.S.; Azab, E.; Gobouri, A.A.; Fouda, A. Green Synthesis of Zinc Oxide Nanoparticles (ZnO-NPs) Using Arthrospira platensis (Class: Cyanophyceae) and Evaluation of their Biomedical Activities. *Nanomaterials* **2021**, *11*, 95. [PubMed]
41. Fouda, A.; Salem, S.S.; Wassel, A.R.; Hamza, M.F.; Shaheen, T.I. Optimization of green biosynthesized visible light active CuO/ZnO nano-photocatalysts for the degradation of organic methylene blue dye. *Heliyon* **2020**, *6*, e04896. [CrossRef]
42. El Golli, A.; Losa, D.; Gioia, C.; Fendrich, M.; Bajpai, O.P.; Jousson, O.; Orlandi, M.; Miotello, A. Advancing solar wastewater treatment: A photocatalytic process via green ZnO/g-C_3N_4 coatings and concentrated sunlight—Comprehensive insights into ciprofloxacin antibiotic inactivation. *J. Environ. Manag.* **2024**, *371*, 123178. [CrossRef]
43. Fouzri, A.; Althumairi, N.A.; Sallet, V.; Lusson, A. Characterization of sol gel Zn_{1-x} Ca_xO thin layers deposited on p-Si substrate by spin-coating method. *Opt. Mater.* **2020**, *110*, 110519. [CrossRef]
44. Mallikarjunaswamy, C.; Lakshmi Ranganatha, V.; Ramu, R.; Udayabhanu; Nagaraju, G. Facile microwave-assisted green synthesis of ZnO nanoparticles: Application to photodegradation, antibacterial and antioxidant. *J. Mater. Sci. Mater. Electron.* **2020**, *31*, 1004–1021. [CrossRef]
45. Thema, F.T.; Manikandan, E.; Dhlamini, M.S.; Maaza, M. Green synthesis of ZnO nanoparticles via Agathosma betulina natural extract. *Mater. Lett.* **2015**, *161*, 124–127. [CrossRef]
46. Sekrafi, T.; Bouricha, B.; Denden, Z.; Tascu, S.; Labidi, A.; Nasri, H.; Dridi, C. Development of Cost-Effective, Selective and Stable Room Temperature Methanol Sensor. *IEEE Sens. J.* **2021**, *21*, 2589–2596.
47. Chu, Y.L.; Young, S.J.; Huang, Y.R.; Arya, S.; Chu, T.T. Highly Sensitive Ethanol Gas Sensors of Au Nanoparticle-Adsorbed ZnO Nanorod Arrays via a Photochemical Deposition Treatment. *ACS Appl. Electron. Mater.* **2025**, *7*, 2327–2338. [CrossRef]
48. Liu, Y.H.; Young, S.J.; Ji, L.W.; Chu, Y.L.; Chang, S.J. High-sensitive ethanol gas sensor using Ag modified ZnO nanosheets. *Talanta Open* **2024**, *10*, 100386.
49. Shinde, R.S.; Khairnar, S.D.; Patil, M.R.; Adole, V.A.; Koli, P.B.; Deshmane, V.V.; Halwar, D.K.; Shinde, R.A.; Pawar, T.B.; Jagdale, B.S.; et al. Synthesis and Characterization of ZnO/CuO Nanocomposites as an Effective Photocatalyst and Gas Sensor for Environmental Remediation. *J. Inorg. Organomet. Polym. Mater.* **2022**, *32*, 1045–1066.
50. Kumar, A.; Kumar, R.; Singh, R.; Prasad, B.; Kumar, D.; Kumar, M. Biosynthesis of ZnO nanoparticles and effect of silver doping in gas sensing characteristics of volatile organic compounds. *J. Coat. Technol. Res.* **2022**, *19*, 685–697.
51. Acharya, T.R.; Lamichhane, P.; Wahab, R.; Chaudhary, D.K.; Shrestha, B.; Joshi, L.P.; Kaushik, N.K.; Choi, E.H. Study on the synthesis of zno nanoparticles using azadirachta indica extracts for the fabrication of a gas sensor. *Molecules* **2021**, *26*, 7685. [CrossRef] [PubMed]
52. Joshi, L.P.; Khatri, B.V.; Gyawali, S.; Gajurel, S.; Chaudhary, D.K. Green Synthesis of Zinc Oxide Nanoparticles Using Ixora Coccinea Leaf Extract for Ethanol Vapour Sensing. *J. Phys. Sci.* **2021**, *32*, 15–26. [CrossRef]
53. Umar, A.; Ibrahim, A.A.; Nakate, U.T.; Albargi, H.; Alsaiari, M.A.; Ahmed, F.; Alharthi, F.A.; Ali Alghamdi, A.; Al-Zaqri, N. Fabrication and characterization of CuO nanoplates based sensor device for ethanol gas sensing application. *Chem. Phys. Lett.* **2021**, *763*, 138204. [CrossRef]
54. Kaur, N.; Zappa, D.; Ferroni, M.; Poli, N.; Campanini, M.; Negrea, R.; Comini, E. Branch-like NiO/ZnO heterostructures for VOC sensing. *Sens. Actuators B Chem.* **2018**, *262*, 477–485. [CrossRef]

55. Deng, X.; Zhang, L.; Guo, J.; Chen, Q.; Ma, J. ZnO enhanced NiO-based gas sensors towards ethanol. *Mater. Res. Bull.* **2017**, *90*, 170–174. [CrossRef]
56. Li, X.Q.; Wei, J.Q.; Xu, J.C.; Jin, H.X.; Jin, D.F.; Peng, X.L.; Hong, B.; Li, J.; Yang, Y.T.; Ge, H.L.; et al. Highly improved sensibility and selectivity ethanol sensor of mesoporous Fe-doped NiO nanowires. *J. Nanopart. Res.* **2017**, *19*, 396. [CrossRef]

Disclaimer/Publisher's Note: The statements, opinions and data contained in all publications are solely those of the individual author(s) and contributor(s) and not of MDPI and/or the editor(s). MDPI and/or the editor(s) disclaim responsibility for any injury to people or property resulting from any ideas, methods, instructions or products referred to in the content.